NAVAL
POSTGRADUATE
SCHOOL

MONTEREY, CALIFORNIA

THESIS

CHARACTERIZATION OF TERAHERTZ BI-MATERIAL SENSORS WITH INTEGRATED METAMATERIAL ABSORBERS

by

Michail Savvas

September 2013

Thesis Co-Advisors:	Gamani Karunasiri Fabio Alves

REPORT DOCUMENTATION PAGE	*Form Approved OMB No. 0704–0188*

1. AGENCY USE ONLY *(Leave blank)*	**2. REPORT DATE** September 2013	**3. REPORT TYPE AND DATES COVERED** Master's Thesis

4. TITLE AND SUBTITLE CHARACTERIZATION OF TERAHERTZ BI-MATERIAL SENSORS WITH INTEGRATED METAMATERIAL ABSORBERS	**5. FUNDING NUMBERS**
6. AUTHOR(S) Michail Savvas	
7. PERFORMING ORGANIZATION NAME(S) AND ADDRESS(ES) Naval Postgraduate School Monterey, CA 93943–5000	**8. PERFORMING ORGANIZATION REPORT NUMBER**
9. SPONSORING /MONITORING AGENCY NAME(S) AND ADDRESS(ES) N/A	**10. SPONSORING/MONITORING AGENCY REPORT NUMBER**

11. SUPPLEMENTARY NOTES The views expressed in this thesis are those of the author and do not reflect the official policy or position of the Department of Defense or the U.S. Government. IRB Protocol number ____N/A____.

12a. DISTRIBUTION / AVAILABILITY STATEMENT Approved for public release; distribution is unlimited	**12b. DISTRIBUTION CODE**

13. ABSTRACT (maximum 200 words)

THz radiation covers the region of the electro-magnetic (EM) spectrum between the microwaves and infra-red (IR), corresponding to frequencies from approximately 100 GHz to 10 THz. Recently, new imaging techniques, which take advantage of the special properties of THz waves, have been developed. Despite the great interest in these new techniques, limitations such as the lack of appropriate detectors and powerful sources are placing the technology in the research domain. The objective of this thesis is to characterize and analyze a set of fabricated bi-material detectors integrated with thin metamaterial films. Different experimental measurements were performed to measure the main figures of merit of the detectors and analyze them. Initially, optical microscopy was used to measure the dimensions of the sensors and stress induced curvature. Then, the thermal response of the sensors was tested and analyzed. The responsivity, the speed of operation and the minimum detected incident power were measured using a quantum cascade laser (QCL), operating at 3.8 THz. The measured experimental data agree well with the theoretical calculated values of the performance parameters.

14. SUBJECT TERMS Terahertz Imaging, Bi-material sensors, Metamaterial Films, Responsivity. Thermomechanical Sensitivity, Speed of Operation, NEP	**15. NUMBER OF PAGES** 61
	16. PRICE CODE

17. SECURITY CLASSIFICATION OF REPORT Unclassified	**18. SECURITY CLASSIFICATION OF THIS PAGE** Unclassified	**19. SECURITY CLASSIFICATION OF ABSTRACT** Unclassified	**20. LIMITATION OF ABSTRACT** UU

NSN 7540–01–280–5500

Standard Form 298 (Rev. 2–89)
Prescribed by ANSI Std. 239–18

THIS PAGE INTENTIONALLY LEFT BLANK

CHARACTERIZATION OF TERAHERTZ BI-MATERIAL SENSORS WITH INTEGRATED METAMATERIAL ABSORBERS

Michail Savvas
Lieutenant, Hellenic Navy
B.S., Hellenic Naval Academy, 2003

Submitted in partial fulfillment of the
requirements for the degree of

MASTER OF SCIENCE IN APPLIED PHYSICS

from the

NAVAL POSTGRADUATE SCHOOL
September 2013

Author: Michail Savvas

Approved by: Gamani Karunasiri
Co-Advisor

Fabio Alves
Co-Advisor

Andres Larraza
Chair, Department of Physics

THIS PAGE INTENTIONALLY LEFT BLANK

ABSTRACT

THz radiation covers the region of the electro-magnetic (EM) spectrum between the microwaves and infra-red (IR), corresponding to frequencies from approximately 100 GHz to 10 THz. Recently, new imaging techniques, which take advantage of the special properties of THz waves, have been developed. Despite the great interest in these new techniques, limitations such as the lack of appropriate detectors and powerful sources are placing the technology in the research domain. The objective of this thesis is to characterize and analyze a set of fabricated bi-material detectors integrated with thin metamaterial films. Different experimental measurements were performed to measure the main figures of merit of the detectors and analyze them. Initially, optical microscopy was used to measure the dimensions of the sensors and stress induced curvature. Then, the thermal response of the sensors was tested and analyzed. The responsivity, the speed of operation and the minimum detected incident power were measured using a quantum cascade laser (QCL), operating at 3.8 THz. The measured experimental data agree well with the theoretical calculated values of the performance parameters.

THIS PAGE INTENTIONALLY LEFT BLANK

TABLE OF CONTENTS

LIST OF FIGURES

LIST OF TABLES

ACKNOWLEDGMENTS

I would like to express my gratitude to my professor, Dr. Gamani Karunasiri for his guidance in my studies in the relevant courses and the completion of my thesis. Also, I would like to sincerely thank Dr. Fabio Alves for his constant and immense support during my research, making this accomplishment possible. Their presence was inspiring and essential throughout the entire process. In addition, I truly thank Brian Kearny, who was always in the lab offering generously his experience, and Dr. Dragoslav Grbovic for his assistance as my professor and his contribution in the whole project. Finally, many thanks to Sam Barone, to Steve Jacobs for providing the technical support, and to Gene Morris for the video recording.

THIS PAGE INTENTIONALLY LEFT BLANK

I. INTRODUCTION

Terahertz (THz) imaging has been an important topic of studies in the recent years, due to its attractive properties for potential applications. Specifically, its nature is non-ionizing (THz photons do not carry enough energy to ionize an electron from an atom or molecule). Therefore, it does not inflict significant damage to human DNA, as do X-ray imaging techniques [1]. Moreover, THz radiation has the ability to penetrate most dry, non-metallic, non-polar materials [2] and simultaneously to resolve details which overmatch the corresponding resolution from sensors operating in the microwave region of the spectrum. However, limitations such as the lack of appropriate detectors and powerful sources are placing the technology in the research domain [3].

Military uses of terahertz waves are constrained, not only by the limited performance of sources and detectors, but also by strong water vapor absorption in the atmosphere which prevents its long range operation at sea level [4]. Therefore, the applications which are of interest to the Navy, cannot yet be implemented, since they require a very strong source for external illumination and hence they are constrained mostly in the security field.

Despite the limitations which arise from the nature of THz radiation, many applications in imaging and communication can be implemented. The high resolution imaging capabilities and rich spectral content have sparked interest not only in military applications [5] but also medical [6], pharmaceutical manufacturing for polymorph detection [7] and non-destructive testing fields [4], aerospace industry etc. Communication and imaging applications can also be performed at high altitudes, since the water vapor concentration decreases rapidly with altitude. Perhaps the greatest potential for new military applications lies in the strong spectral dependence of the interaction with materials, where resonant absorption by the molecular structure of targets provides information on their composition, and hence the target identity, not readily available by other remote sensing methods [4]. A wide variety of techniques is available for security screening to detect the presence of various threats, such as weapons containing a small amount of metal, ceramic explosives, explosive materials, chemical and biological threats [8].

Nevertheless, for real-time imaging applications, a sensor with a relatively high speed of operation and sensitivity would be required. Despite the great interest in this area of the electromagnetic spectrum, the design and fabrication of sensors with those characteristics is still only in the research stage.

Recently, a novel approach has been used by researchers at the Sensor Research Lab of the Naval Postgraduate School (NPS), using micro-electromechanical systems (MEMS) bi-material sensors with structural metamaterial layers to drastically increase THz sensitivity. Bi-material sensors are very convenient because they allow the use of external optical readout, avoiding complex integrated microelectronics configurations. Metamaterials are artificial materials whose properties can be tailored by design to fill the gaps of natural materials. They can be designed to absorb nearly 100% of THz radiation in specific frequencies, which cannot be found in natural occurrences. The combination of metamaterials and MEMS bi-material sensors has shown to be very attractive for real-time THz imaging [9].

The NPS Sensor Research Lab group has designed and fabricated sensors, which are "made of materials that are fabrication-friendly, exhibit low residual stress, have very different thermal expansion coefficients and strong THz absorption. Configurations should have a large absorption area, good thermal isolation to increase sensitivity and provide a reflective surface for optical readout. All of these requirements are intrinsically interdependent making the optimization of the final choice highly dependent on the application. Nonetheless, the quest to achieve high performance THz bi-material detectors starts with $d\theta/dt$, defined by the bi-metallic effect and η, which is maximized by the integration of metamaterial structures" [2].

In order to optimize the integration of metamaterials in MEMS bi-material sensors, different configurations were fabricated where metamaterials and bi-material characteristics were varied to allow the observations of their effects in the overall sensor response. In this context, **the objective of this thesis is to characterize and analyze the fabricated sensors and provide feedback to optimize future designs.**

To achieve this goal, the research work reported in this thesis was conducted according to the methods described in the following paragraph:

Initially, the dimensions and geometrical details of the detectors were observed and measured using optical microscopy. Subsequently, bi-material response and figures-of-merit were experimentally determined. The bi-material response of the sensors was measured using a heat chuck for a range of temperatures from 295 to 314 K. Then a quantum cascade laser (QCL) operating at 3.8 THz was used as an illumination source to determine THz characteristics of the sensors. Through this experiment, operating parameters of the sensors, such as the responsivity, the speed of operation and the minimum detectable power, were measured. Then, the figures of merit mentioned above were analytically estimated to allow for the assessment of the design methods.

In summary, eight different configurations of bi-material based sensors were characterized and analyzed to allow optimization of future designs aimed at specific applications.

THIS PAGE INTENTIONALLY LEFT BLANK

II. THEORETICAL BACKGROUND

A. TERAHERTZ RADIATION AND TERAHERTZ IMAGING

THz radiation covers the part of the electro-magnetic (EM) spectrum between the microwaves and infrared (IR), which corresponds to wavelengths from 30 μm to 3 mm. This results in the sharing of some characteristics from both of these regions.

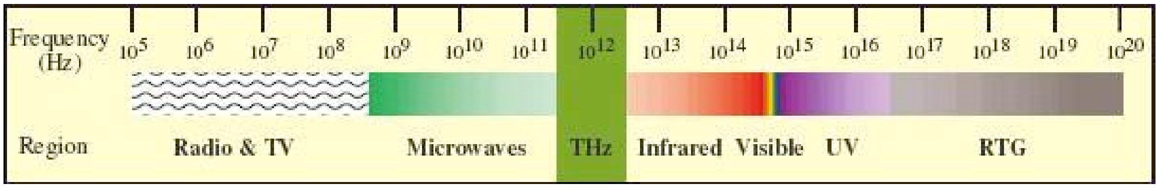

Figure 1. EM spectrum with highlighted THz region.

Detection and spectroscopy in the THz spectral range have been reported to include several different approaches. These include the use of different detectors and techniques, such as microbolometer and pyroelectric based thermal detectors, photoconductive dipole antennas, Fourier transform terahertz spectroscopy and time domain spectroscopy [10], [11]. Real-time THz imaging has been demonstrated using conventional, microbolometer-based imagers optimized for infrared (IR) wavelengths (8–12 μm) coupled with a QCL as an illumination source [2], [12], [13]. Limitations, such as the low sensitivity of the microbolometer cameras in the THz region, motivated the development of more sensitive detectors. The use of bi-material sensors has shown many advantages, which make it a potential solution for THz imaging.

B. PRINCIPLE OF OPERATION OF BI-MATERIAL SENSORS

The micro-electromechanical, bi-material based sensor relies on the deflection of bi-material structures under rising temperature due to electromagnetic radiation absorption [9]. The potential of employing external optical readout is what makes this way of detection attractive [14], [15].

A typical bi-material THz detector has three main components: (a) a metamaterial absorber, (b) bi-material legs (microcantilevers) and (c) a thermally insulating anchor as illustrated in Figure 2 (a).

The absorber is responsible for capturing the incoming THz radiation and converting it into heat. The heat is then transmitted via the bi-material legs and anchors to the substrate. During this process the bi-material legs and the absorber attached to it, deflect as shown in Figure 2(b). The anchor connects the bi-material legs to the substrate and also thermally isolates the structure from the Si substrate. The substrate acts as a heat sink, allowing the sensor to return to its unperturbed position when incoming radiation is terminated [9]. In addition, an adequate reflective surface is necessary to allow optical readout.

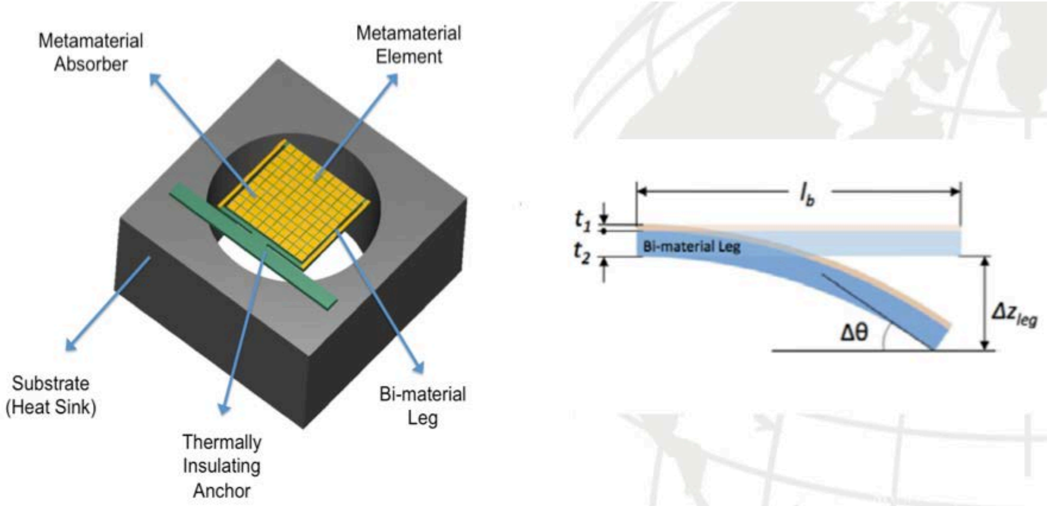

Figure 2. Bi-material Sensor (a) 3D view of the THz bi-material sensor with metamaterial absorber, fabricated on a Si substrate (b) Side view of an isolated bi-material leg connected to central absorber. From [2].

In Figure 2(b) the metal (*Al*) coating is shown with thickness t_1, in pink, while the structural layer, made of silicon-rich silicon oxide (SiO_x), with thickness t_2 is shown in blue. These two materials compose the bi-metallic leg and have different thermal expansion coefficients. Therefore, they undergo expansion at different rates with the same temperature change, resulting in bi-material beam bending.

C. METAMATERIAL FILMS

The use of metamaterial films as absorbers, integrated with bi-material sensors, exhibits several advantages. Their absorption characteristics were studied in [16] and [17] and showed that an absorber with absorption near 100% can be designed for the desired frequency. The metamaterial layer used in the studied THz sensors is comprised of a periodic array of Al square elements separated from an Al ground plane by the SiO_x layer, as schematically illustrated in Figure 3. Such a combination allows matching to the free space impedance at specific frequencies, eliminating the reflection, while the ground plane prevents transmission which results in nearly 100% absorption. In addition, the ground plane of the metamaterial acts as a mirror for optical readout of the deflection.

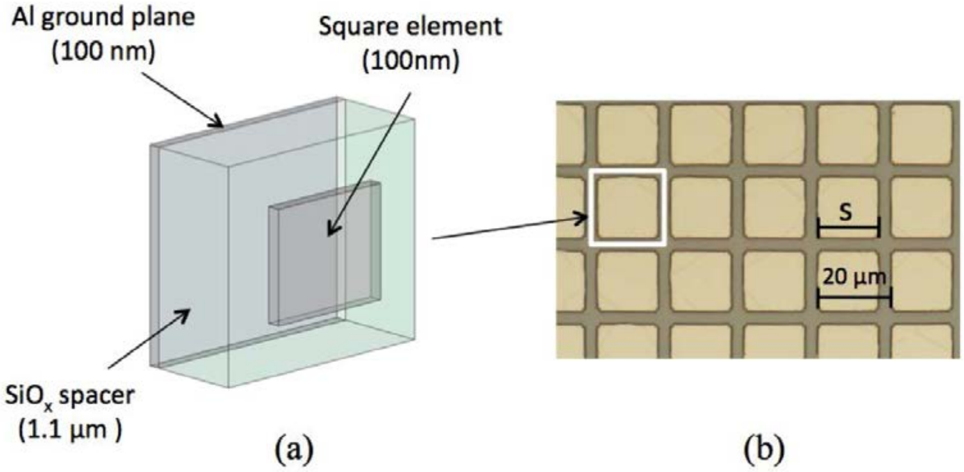

Figure 3. Metamaterial Absorber (a) Schematics of a metamaterial unit cell, consisting of a 100 nm Al ground plane, a 100nm square element, separated by a 1.1.µm SiO_x layer. (b) Metamaterial test structures with 20µm period and varying square dimension (s), fabricated in a Si substrate. From [17].

The fraction of the incident power absorbed by the sensor is represented by the absorption efficiency *η*. The absorption for three metamaterial structures with different square sizes (s = 17, 18 and 19 μm) and the same repetition period (20 μm) was experimentally measured in [2] and the results are shown in Figure 4.

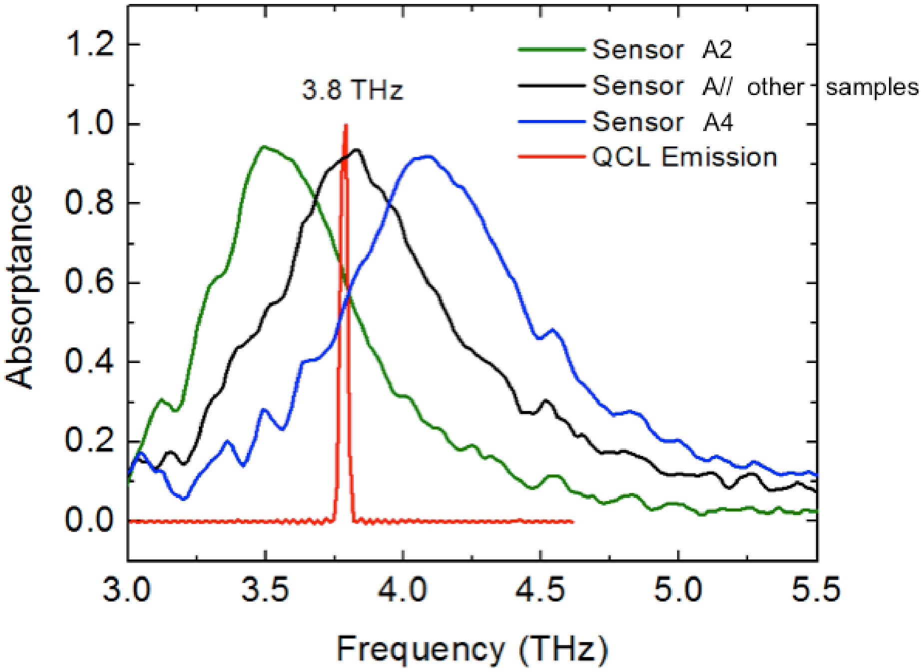

Figure 4. Absorption measurements of metamaterial with square sizes of 19 μm (A2), 17 μm (A4) and 18 μm (A1, A3, A5-A8) with the same repetition period of 20 μm. The red line is the normalized power of the QCL used in this thesis characterization work. From [2].

From the data in Figure 4, it is possible to extract the absorption efficiency of all studied sensors at the illuminating QCL frequency (see Table 1 at the end of this section).

D. DESCRIPTION OF THE SENSORS

To optimize the operation of a bi-material sensor, two main choices have to be considered, the materials and the configuration. For this study, “the combination of SiO_x and *Al* (both standard MEMS materials) to maximize thermomechanical sensitivity $d\theta/dT$, while simultaneously alleviating some of the excessive residual stress related deformation, observed in the sensors fabricated in [9] was selected. Furthermore, SiO_x and Al exhibit electro-optical properties that are suitable for fabricating highly efficient metamaterial absorbers” [2].

Several bi-material sensors with metamaterial absorbing films were fabricated using $Al/SiO_x/Al$ layers on a *Si* wafer. The thickness of the Al layers, both for the ground plane and the square element, was 100 nm, while the thickness of the Al layer of the bi-material legs (t_1 in Figure 2 (b)) is 170 nm. The thickness of the intermediary layer of SiO_x (t_2) is 1.1 μm.

The sensors are designed with different configurations, and in the case of the same configuration they have different metamaterial parameters (square size and pitch). Therefore, the total absorbing area differs between the configurations. The length of the legs also varies depending on the configuration, while their width remains the same. The width of the anchors is constant, but in some configurations the anchor has been designed to consist of two identical regions with a gap in between them. Micrographs of the components of sensor A1 are depicted in Figure 5.

As mentioned before and depicted in Figure 4, a structure with square size $18x18\mu m^2$ gives absorption efficiency of around η~95%, at the 3.8 THz. The sensors with different square sizes appear to have a significantly different efficiency of absorption (see Figure 4). The geometrical data and the corresponding absorption efficiency for each configuration are listed in Table 1, later in this section.

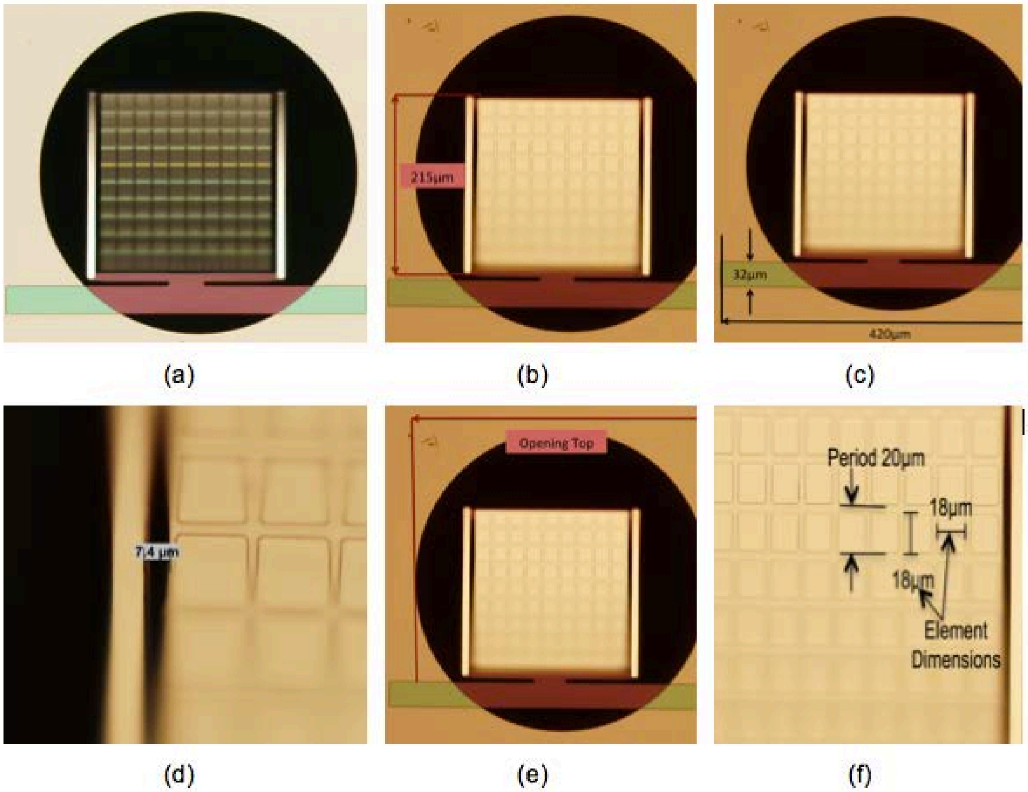

Figure 5. Micrographs of sections of sensor A1 (a) top view, (b) bi-material leg, (c) anchor, (d) gap between legs and absorbing area, (e) trench in the substrate, and (f) metamaterial dimensions.

Figure 6 shows the micrographs of the top view of the eight bi-material sensors which are studied in this thesis. In most of the cases, the sensors are out of focus because the absorbing area is tilted due to intrinsic residual stress.

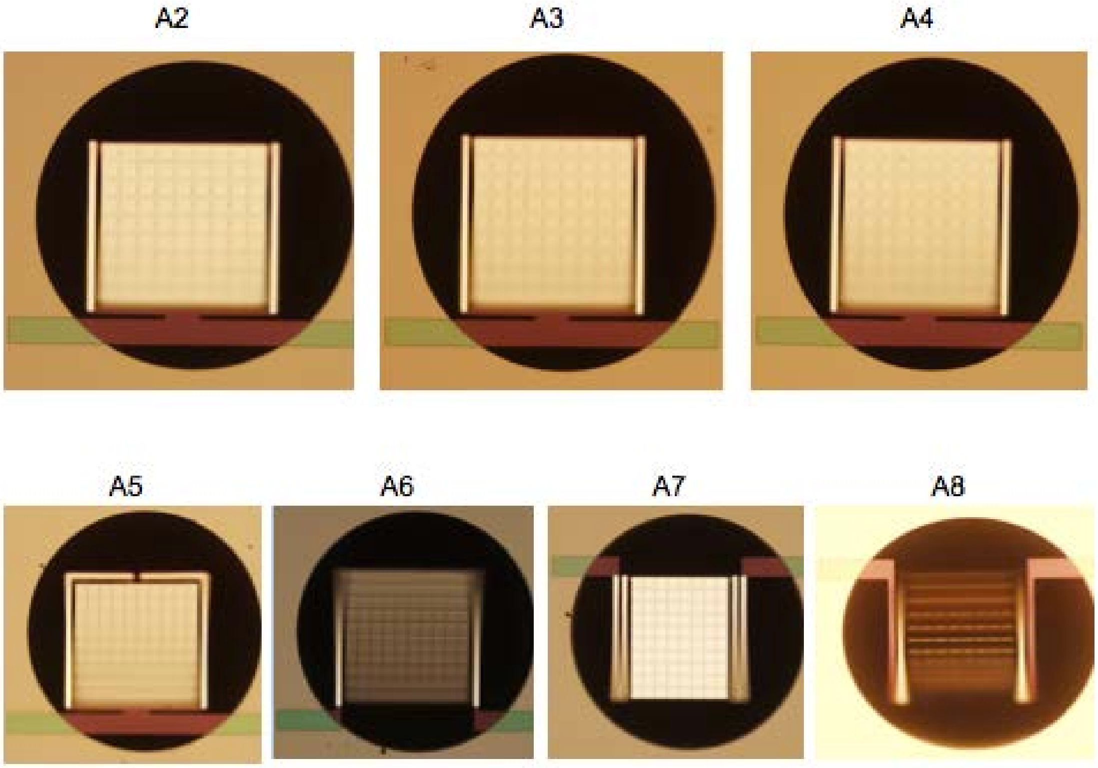

Figure 6. Micrographs of the top view of the studied detectors. Sensors A2, A3 and A4 have the same configuration as A1. Sensors A2 and A4 have larger and smaller square sizes, respectively. Sensor A5 has longer bi-material legs, which are connected to the absorber at the top center. Sensor A6 has two separate anchors, which are separated by a gap. Sensor A7 has two double bi-material legs with anchors similar to that of A6. In sensor A8, the two exterior legs are non-metallized and form part of the anchor.

The detectors A1 to A4 have the same configuration, however, with different geometrical details. Specifically, they have side-connected legs and one-piece thermal insulating anchor. The metamaterial absorbers of sensorsA1 and A3 have the same square size $(18x18\mu m^2)$ and hence the same absorption efficiency η. Sensors A2 and A4 have larger $(19x19\mu m^2)$ and smaller $(17x17\mu m^2)$ squares, respectively, which in both cases negatively affects their efficiency, as explained in Chapter II, Section C. This fact is expected to affect the responsivity of the sensors. All the first four configurations have an equal central absorbing area of $200x200\mu m^2$.

In the sensor A5, there is an additional extension of metalized legs to get more bimetallic effect. Its square size is equal to that of sensors A1 and A3, $18x18\mu m^2$, but because of the extension of the legs, its central absorbing area is decreased to $200x180\mu m^2$.

Sensor A6 is of the same design as the first four, but with a different size thermal insulating anchor, which in this case consists of two individual parts separated by a 212 *µm* gap. This difference is expected to affect the response time of the sensor. The size of its squares and the total central surface is equal to A1.

The sensors A1 to A6 have bi-material legs of the same length equal to 214 *µm*. The width of the legs is also the same in all the sensors.

Sensor A7 was designed to have two bi-material legs interconnected in opposite directions. In this configuration, the thermal deformation of one leg compensates for the other; therefore there is almost no angular displacement on the central part. Hence, it is expected to be the least sensitive among all the sensors, because of its minimum deflection under increasing temperature. Moreover, its metamaterial central region is smaller than that of the rest of the sensors specifically, $200x160\mu m^2$, and the length of bi-material legs is 200 *µm*. The thermally insulating region, which is in two parts as in the case of A6, is attached the top sides of the legs. The gap in this case is 200 *µm*. The square size is $18x18\mu m^2$which corresponds to absorption efficiency of η ~0.95.

Sensor A8 has a similar design and dimensions to sensor A7 but the exterior legs are non-metallized and constitute part of the anchor. In this case, the longer anchor is expected to reduce the thermal conductance and therefore increase the time constant. Its gap is also 200 *µm* and its absorbing area is smaller than that of sensor A1, $200x160\mu m^2$, which is expected to affect the sensitivity. It has the same square size, efficiency and length of the bi-material legs as in A7. The detailed dimensions of the detectors are presented in Table 1:

Sensor	*A1*	*A2*	*A3*	*A4*	*A5*	*A6*	*A7*	*A8*
Geometrical Details								
Central Absorber (μm^2)	200x200	200x200	200x200	200x200	200x180	200x200	200x160	200x160
Square element (μm^2)	18x18	19x19	18x18	17x17	18x18	18x18	18x18	18x18
Absorption Coefficient	0.95	0.64	0.95	0.59	0.95	0.95	0.95	0.95
Bi-material leg length (μm)	214	214	214	214	306	214	200	200
Gap length between anchor regions (μm)	--	--	--	--	--	212	200	200

Table 1. Detailed dimensions of the main parts and characteristics of the sensors. The corresponding absorption efficiency is obtained exclusively by the square element size.

E. FIGURES OF MERIT

The most significant figures of merit of bi-material sensors for imaging applications are the thermomechanical sensitivity, the speed of operation, the responsivity and the Noise Equivalent Power (NEP) [2].

The thermomechanical sensitivity can be defined as the angular deflection due to temperature change $d\theta/dT$. This characteristic depends basically on the bi-metallic effect and can be increased by properly selecting the bi-material layer thicknesses. The linear displacement, Δz_{leg}, of the tip of a cantilever consisting of two material layers, as depicted in Figure 2(b), was first quantified by Timoschenko [18]. In the case of the studied sensors, the linear displacement Δz_{leg} is much smaller than the length l_b of the bi-material leg, allowing for the estimation of the angular deflection (Δθ) by dividing Δz_{leg} by l_b. When the leg is connected to a free standing absorber, as shown in Figure 2(b), the sensor deflection is twice the leg deflection. The thermomechanical sensitivity is given by [2]:

$$\frac{d\theta}{dT} = 6l_b(t_1 + t_2)t_2^{-2}(4 + 6\frac{t_1}{t_2} + 4\frac{t_1^2}{t_2^2} + \frac{t_1^3}{t_2^3}\frac{E_1}{E_2} + \frac{t_2}{t_1}\frac{E_2}{E_1})^{-1}(\alpha_1 - \alpha_2), \tag{1}$$

where *t* is the thickness, *α* is the thermal expansion coefficient and *E* is the Young's modulus. The indices 1 and 2 represent the metal (Al) and the dielectric structure (SiO_x) respectively.

The sensor's speed of operation is typically described by the thermal time constant of the sensor, which determines the reaction time of the sensor. For imaging applications it has to be as low as possible [19]. It is defined as from [20]:

$$\tau = \frac{C}{G} \tag{2}$$

where C is the heat capacitance, and G is the thermal conductance of the sensor.

The thermal capacitance can be estimated using the expression:

$$C = c_{th}\rho A_s t \tag{3}$$

where c_{th} is the heat capacity dependent on the material properties, *ρ* is the material density and *t* is the structure thickness. A_s is the corresponding surface area.

In our research the total heat capacitance was calculated as the sum of the heat capacitances of the three main sections of the sensors. For the top part of the central absorbing area, the metamaterial elements cover 80% of the total surface and have a thickness of 100*nm*, while the other layers SiO_x and Al (ground plane) cover 100% of the area with a thickness 1.1*μm* and 100*nm*, respectively. In the case of the bi-material legs, the C_{leg} was calculated as a sum of the heat capacitances of the Al top part, with thickness 170 nm, and the SiO_x layer with a thickness of 1.1*μm*. Finally, for the anchor, the only material used there was the SiO_x, which was 1.1*μm* thick.

The heat conduction to the surroundings consists of several components which can be represented by total thermal conductance, $Gtot$.[19] The three primary components of thermal conductance:

1. G_b , is the thermal conductance to the heat sink,
2. G_{rad}, is the thermal conductance via the radiation,
3. G_{conv}, is the thermal conductance via the convection.

The thermal conductance to the heat sink was estimated using the expression from [2]

$$G_b = g_{th} \frac{A_c}{l} \tag{4}$$

where $g_{th}$is the thermal conductivity, A_c is the cross sectional area and *l* is the length.

Since the thermal conductance is defined as the inverse of thermal resistance, the inverse of the total thermal conductance via the body was calculated as the sum of the inverses of each individual part of the anchor with different cross sectional areas. The metal layers were considered thermal shorts due to their high thermal conductivity in comparison to the SiO_x.

The thermal conductance via the radiation was estimated using the expression from [19]

$$G_{rad} = 4\varepsilon_{top} A_s \sigma T_s^3 + 4\varepsilon_{bot} A_s \sigma T_s^3 \tag{5}$$

where ε_{top} and ε_{bot} is the emissivity of the top and the bottom part, respectively, A_s is the surface area, $\sigma = 5.670373\times10^{-8}$ $W\ m^{-2}\ K^{-4}$ is the Stefan Boltzmann constant and $T_S = 300\ K$ is the room temperature. For the top central metamaterial surface, the thermal conductance was calculated using emissivity of metamaterial $\varepsilon_{met} = 0.5$, while for the bottom part, which is the *Al* ground plane, the emissivity used was $\varepsilon_{Al} = 0.05$. Since the anchors are made of SiO_x uniformly, the emissivity used for both the top and the bottom surfaces was $\varepsilon_{SiO_x} = 0.8$. The same factor was used for the bottom surface of the bi-material legs and for the top surface of its two exterior non-metallized legs in sensor A8. For the top surfaces of its two interior metallized legs the emissivity ε_{Al} was used. The heat dissipation due to convection was neglected, since the sensors were operated in a low pressure vacuum chamber.

The thermal conductance due to radiation and the body were found to be of the same order of magnitude, and the total thermal conductance of the sensor was calculated as the sum of the two.

The material properties that were used for the above calculations are listed in Table 2.

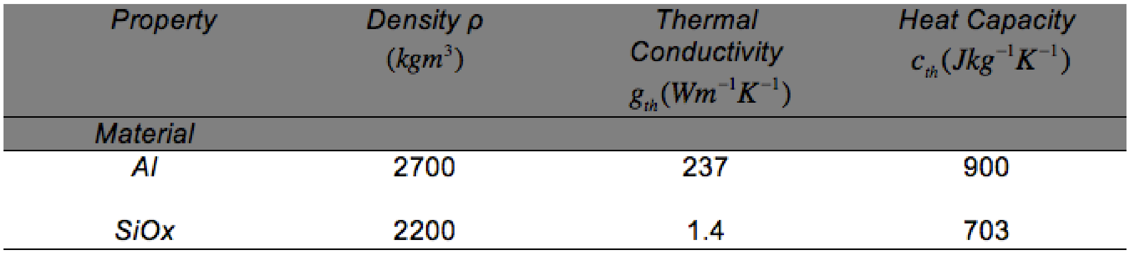

Property	*Density ρ* (kgm^3)	*Thermal Conductivity* $g_{th}(Wm^{-1}K^{-1})$	*Heat Capacity* $c_{th}(Jkg^{-1}K^{-1})$
Material			
Al	2700	237	900
SiOx	2200	1.4	703

Table 2. Material properties of the layers used for fabricating the sensors.

The responsivity ($d\theta/dP$) of a bi-material sensor is defined as the angular deflection per unit power, given by the following equation from [2]:

$$R = \frac{d\theta}{dP} = \frac{\eta}{G}\frac{d\theta}{dT} \tag{6}$$

In Equation (6), the efficiency (η) depends only on the metamaterial absorption at the frequency of the illumination source. Most of the sensors studied in this thesis have the efficiency η~95% with some variations, as was shown in Sections C and D of this chapter.

For bi-material sensors, noise equivalent power (NEP) is defined as the incident radiant power that produces a signal equal to the detector's root mean square (rms) noise [21], [22]. The primary noise sources intrinsic to the detectors are temperature fluctuations, background fluctuations and thermomechanical noise, while the external sources of noise are the illumination source fluctuations, the readout laser fluctuation, mechanical vibrations of the cooling system and the vacuum chamber, as well as the readout sensor noise.

In this thesis, we estimate the intrinsic noise and measure the total noise of the sensor/source/readout system. The spontaneous fluctuation in angular deflection (deg) of the absorbers caused by temperature fluctuations is given by

$$\left\langle \delta\theta_{TF}^{2} \right\rangle^{1/2} = \frac{\left(d\theta/dP\right)T\sqrt{4k_B GB}}{\eta} \tag{7}$$

where T is the sensor temperature, k_B is the Boltzmann constant, G is the total thermal conductance and B is the bandwidth, which can be set to unity. The background fluctuation noise can be obtained by replacing the total thermal conductance in Equation (7) by thermal conductance via radiation loss of heat. The angular deflection (deg) due to thermomechanical noise, knowing that the detector operating frequency is much slower than the mechanical resonances (few kHz), is given by

$$\left\langle \delta\theta_{TM}^{2} \right\rangle^{1/2} = \frac{360}{\pi l_b}\sqrt{\frac{4k_b TB}{Qk\omega_0}} \tag{8}$$

where Q is the quality factor, k is the stiffness and ω_0 is the resonant angular frequency of the mechanical structure [2].

In this thesis several different configurations with different geometrical details are studied. The measured characteristics and their comparison with the calculations are presented in the next chapter.

III. COMPARISON AND ANALYSIS OF CALCULATED AND MEASURED DATA

A. THEORETICAL ESTIMATION OF THE FIGURES OF MERIT

1. THERMOMECHANICAL SENSITIVITY

Using Equation 1 (see Chapter II) and the dimensions of the sensors, the angular deflection was calculated analytically for each sensor and is listed in Table 3.

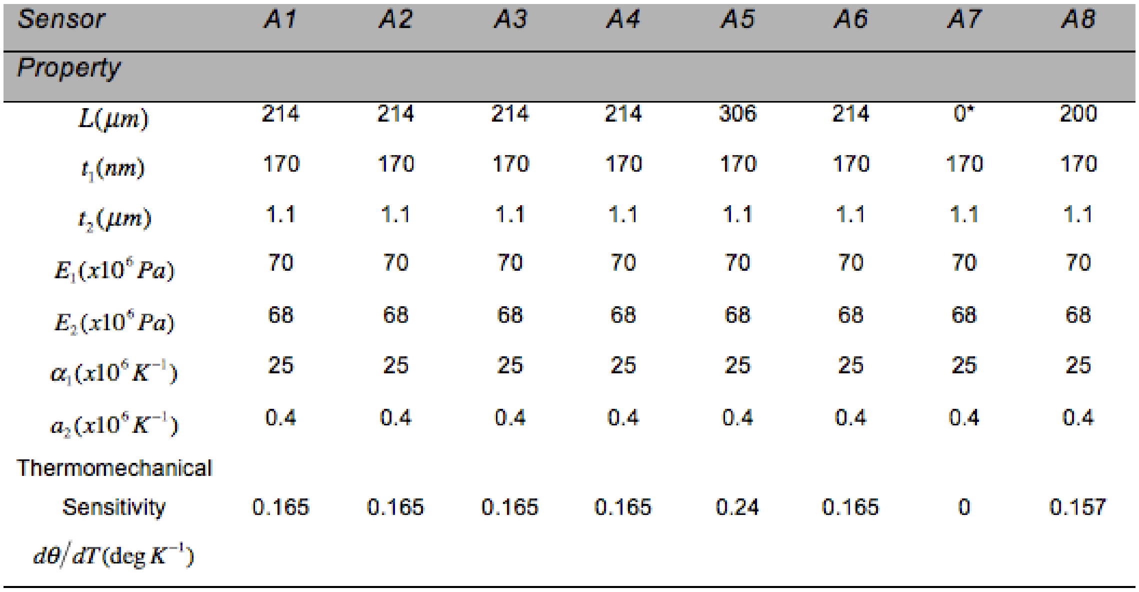

Sensor	A1	A2	A3	A4	A5	A6	A7	A8
Property								
$L(\mu m)$	214	214	214	214	306	214	0*	200
$t_1(nm)$	170	170	170	170	170	170	170	170
$t_2(\mu m)$	1.1	1.1	1.1	1.1	1.1	1.1	1.1	1.1
$E_1(x10^6 Pa)$	70	70	70	70	70	70	70	70
$E_2(x10^6 Pa)$	68	68	68	68	68	68	68	68
$\alpha_1(x10^6 K^{-1})$	25	25	25	25	25	25	25	25
$a_2(x10^6 K^{-1})$	0.4	0.4	0.4	0.4	0.4	0.4	0.4	0.4
Thermomechanical Sensitivity $d\theta/dT(\deg K^{-1})$	0.165	0.165	0.165	0.165	0.24	0.165	0	0.157

Table 3. Dimensions of the sensors, required for the theoretical calculation of thermomechanical sensitivity, using Equation (1). The only parameter defining the difference between the sensors' angular deflection is the length of the bi-material legs. *As explained before, sensor A7 was designed to have two bi-material legs interconnected in opposite directions. In this configuration, the thermal deformation of one leg compensates for the other resulting in no appreciable angular displacement on the central part.

Sensors A1 to A4 and A6 have the same theoretical value of thermomechanical sensitivity due to the same length of the bi-material legs. Sensor A5 has longer bi-material legs, which increases its theoretical sensitivity.

Sensor A8 has lower theoretical sensitivity than A1, because of the shorter bi-material legs.

2. SPEED OF OPERATION

Using Equations (3) to (5) from Chapter II, the sensor dimensions and the data from Table 2, the thermal capacitance, C, and the thermal conductance, G, were calculated for each individual sensor. Then, using Equation (2), the theoretical values of the time constant were also calculated and tabulated.

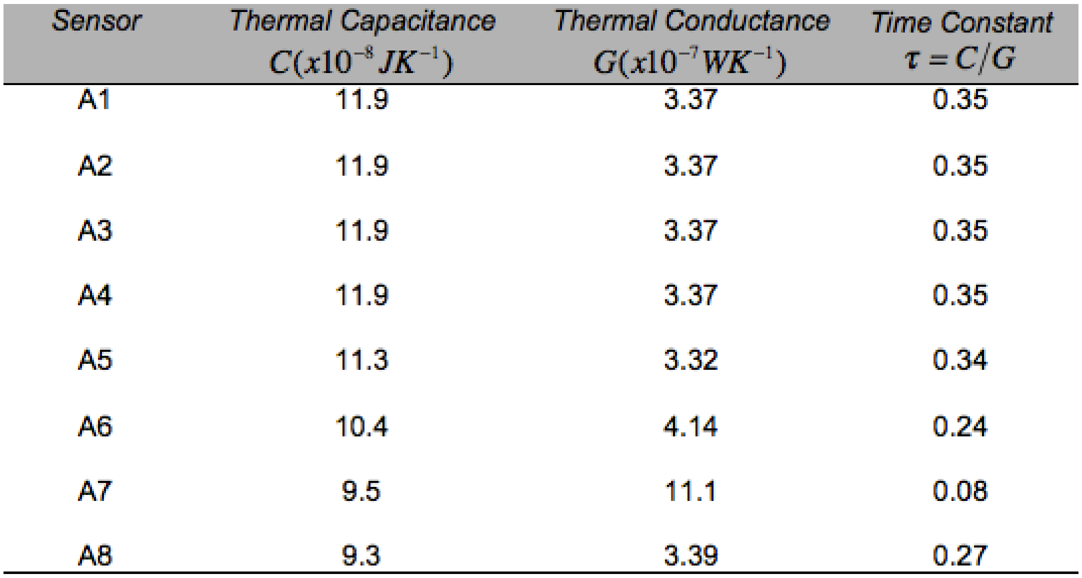

Sensor	*Thermal Capacitance* $C(x10^{-8}JK^{-1})$	*Thermal Conductance* $G(x10^{-7}WK^{-1})$	*Time Constant* $\tau = C/G$
A1	11.9	3.37	0.35
A2	11.9	3.37	0.35
A3	11.9	3.37	0.35
A4	11.9	3.37	0.35
A5	11.3	3.32	0.34
A6	10.4	4.14	0.24
A7	9.5	11.1	0.08
A8	9.3	3.39	0.27

Table 4. Theoretical estimation of thermal capacitance *C*, thermal conductance *G* and time constant τ of the sensors, using Equations (2) to (5) and data from Table 2.

Sensors A1 to A5 have a similar theoretical time constants. This is due to the fact that they have the same anchor configuration and same size of central absorbing area, except A5, which has a slightly smaller area. This results in a lower time constant. Sensor A6 has higher thermal conductance because of the shorter anchor.

Sensors A7 and A8 have lower thermal capacitance and greater thermal conductance than the other sensors. This is expected due to the smaller size of the anchor, especially for sensor A7, and also the smaller absorbing area of both sensors.

Sensor A5 has a time constant similar to the sensors A1 through A4, although it has a smaller absorbing area. This is due to the longer legs that provides smaller thermal conductance.

3. RESPONSIVITY

The theoretical values of the responsivity of the sensors were calculated using Equation (6) in Chapter II and the data from Table 2 (angular deflections). The results are presented in Table 5.

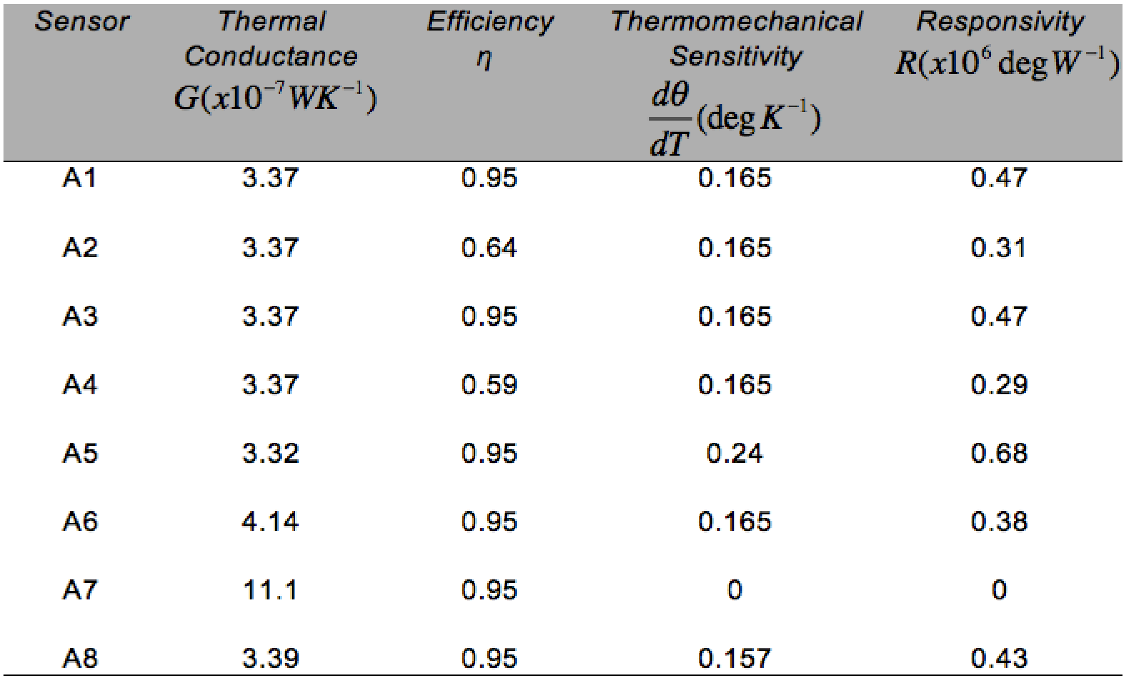

Sensor	*Thermal Conductance* $G(x10^{-7}WK^{-1})$	*Efficiency* η	*Thermomechanical Sensitivity* $\frac{d\theta}{dT}(\deg K^{-1})$	*Responsivity* $R(x10^{6}\deg W^{-1})$
A1	3.37	0.95	0.165	0.47
A2	3.37	0.64	0.165	0.31
A3	3.37	0.95	0.165	0.47
A4	3.37	0.59	0.165	0.29
A5	3.32	0.95	0.24	0.68
A6	4.14	0.95	0.165	0.38
A7	11.1	0.95	0	0
A8	3.39	0.95	0.157	0.43

Table 5. Analytical calculation of the responsivity of the sensors using Equation (6) and data from Table 3.

As can be seen in Table 5, sensors A2 and A4 have a significantly lower theoretical responsivity compared to sensors A1 and A3 because of their lower absorption efficiency.

Sensor A5 has the highest theoretical value of responsivity among all the sensors due to its high absorption efficiency (~95%) and the longest legs, which increase its thermomechanical sensitivity.

Sensor A6 has a lower responsivity than A1, although both have equal absorption efficiencies. This is due to A6's smaller cross sectional area of legs, which results in the increase of its thermal conductance.

Sensor A7 has no theoretical responsivity due to the reasons already explained.

Sensor A8 has a similar responsivity to A1, because its two exterior non-metallized legs contribute to the increase of thermal insulation similar to the sensor A1's anchor. Since they have the same absorption efficiencies, they exhibit almost the same responsivity.

B. EXPERIMENTAL MEASUREMENTS AND DATA

1. OPTICAL MICROSCOPE MEASUREMENTS

First, the geometrical dimensions of the sensors were measured using optical microscopy to verify the accuracy of the fabrication's process. Micrographs showing the top view of all the sensors and the components of the sensor A1 are depicted in Figures 5 and 6 in Chapter II. The measured dimensions are listed in Table 6.

Sensor	*Central Absorber* (μm^2)	*Metamaterial Element* (μm^2)	*Intrinsic Deflection of Central Absorber (deg)*	*Intrinsic Deflection of Metallized Legs (deg)*
A1	200x200	18x18	7.5	5
A2	200x200	19x19	10	2.4
A3	200x200	18x18	10.5	3
A4	200x200	17x17	13	4.5
A5	200x180	18x18	11	3.7
A6	200x200	18x18	19	9.5
A7	200x160	18x18	0.9	7
A8	200x160	18x18	28	--

Table 6. Geometrical details and intrinsic deflections of the detectors due to the residual stress.

The measured dimensions are in good agreement with the designed parameters showing that the fabrication process, described in [2] is highly reliable.

The intrinsic angular deflection was calculated using the arctangent of the measured vertical deflection over the absorber’s lateral dimension. The measured vertical deflection is the number of deviations of the adjustment knob of the microscope needed to focus the two edges of the absorber along the lateral dimension. Each deviation corresponds to 1 μm. The lateral dimension was in every case equal to 200 μm for the central absorber, 214 μm for A1-A6 and 200 μm for A7-A8 for the bi-material legs.

2. THERMAL RESPONSE MEASUREMENTS

The thermal response $({}^{d\theta}\!/_{dT})$ of the sensors was measured by attaching it to a flat resistive heating element and varying the temperature from 295 to 306

K, and, in the case of sensor A7, up to 314 K. This approach provides thermal response similar to that which would be obtained if only the absorber was uniformly heated using THz since the temperature gradient in the bi-material legs is less than 5% compared to that of the absorber (central element) and the substrate (heat sink). Therefore, the legs can be assumed to be thermally shorted, allowing the measurement of the thermal response by uniformly heating the sensors [2].

The displacement of beam of light from a laser diode reflected from the back side of the absorbers was projected on a screen to measure the deflection of absorber as the temperature changed. Knowing the beam path length, the angular displacement of the absorbers was estimated. Figure 7 shows a schematic diagram of the experimental setup.

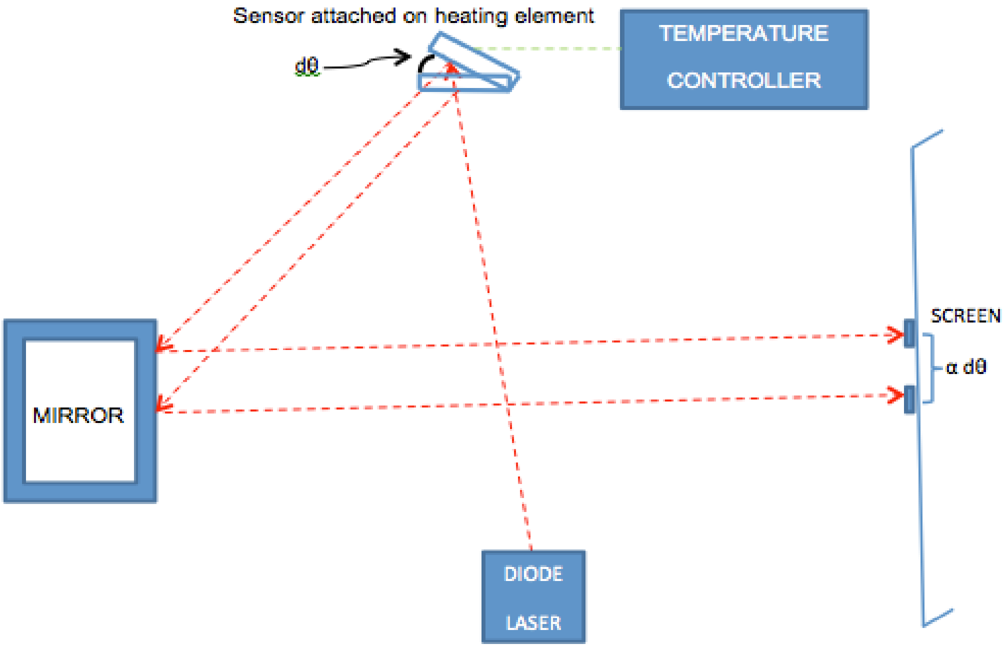

Figure 7. Schematic diagram of thermal response measurement system. The temperature of the sensor is set using the heating element and temperature controller. The diode laser illuminates the back side of the absorber. The deflection of the reflected beam from the back side of the absorber is projected onto a screen.

Figure 8 shows a picture of the actual experimental setup.

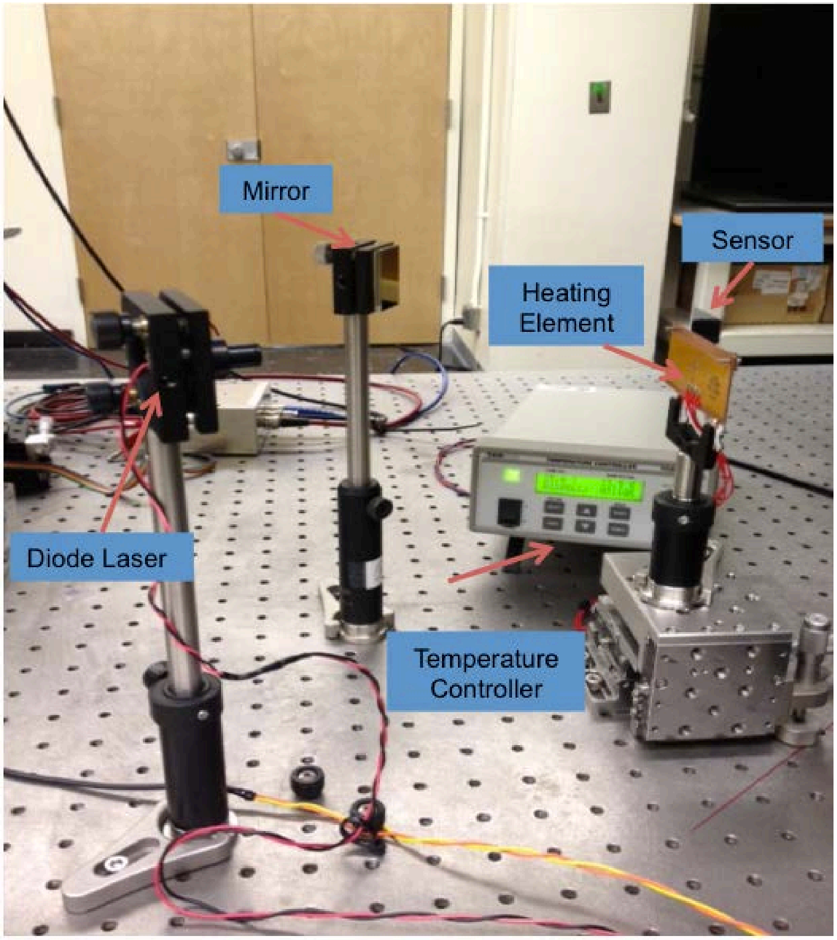

Figure 8. Actual experimental setup used for the thermal response measurement.

Figure 9 shows the measured angular displacement as a function of temperature for the sensor A1. The solid line is the linear fit, showing that the response of the sensor in this temperature range is nearly linear. The same procedure was adopted for the rest of the sensors and the slopes of the linear fits are listed in Table 7.

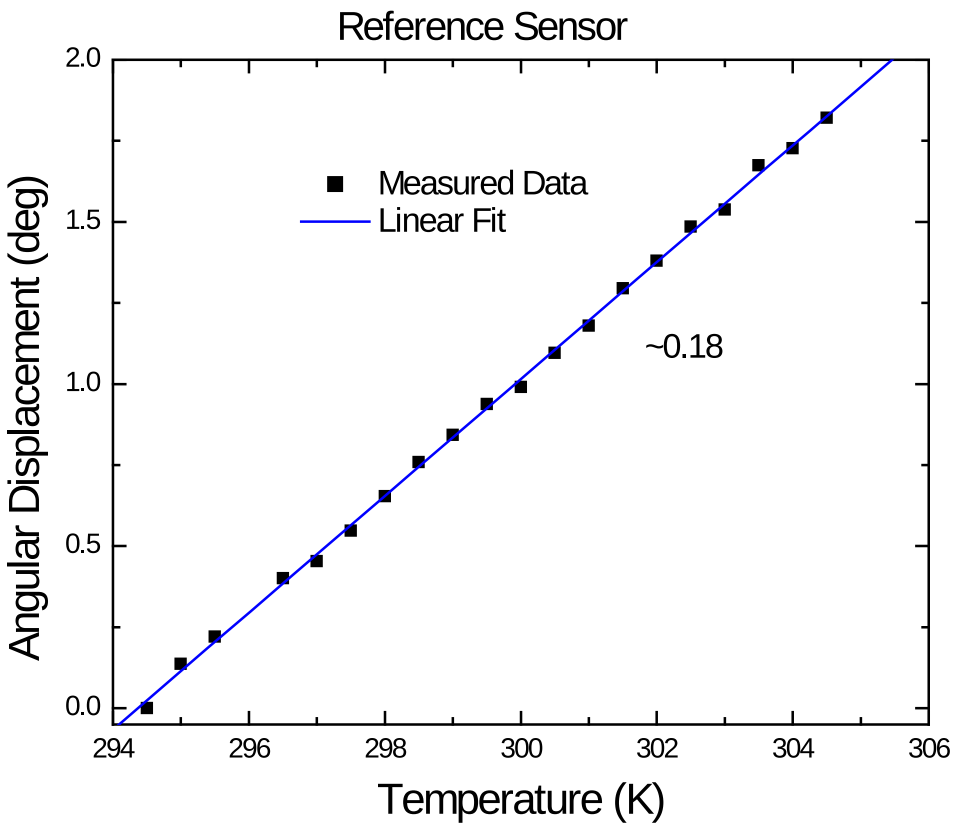

Figure 9. Angular displacement due to changing temperature of sensor A1. The slope of the plot represents the thermomechanical sensitivity of the sensor. provide units for the 0.18 on the figure)

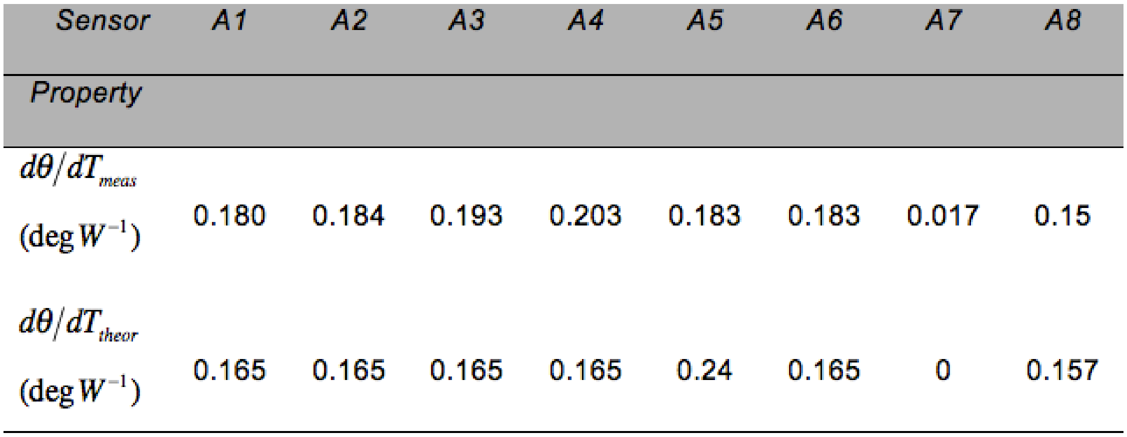

Sensor	A1	A2	A3	A4	A5	A6	A7	A8
Property								
$d\theta/dT_{meas}$ ($\deg W^{-1}$)	0.180	0.184	0.193	0.203	0.183	0.183	0.017	0.15
$d\theta/dT_{theor}$ ($\deg W^{-1}$)	0.165	0.165	0.165	0.165	0.24	0.165	0	0.157

Table 7. Comparison between analytically calculated and experimental values of thermomechanical sensitivity *(dθ/dT)* of the sensors.

As can be seen in Table 7, the sensitivity of sensor A1 is 0.18 *deg/K*. The other sensors, except sensor A7, have approximately similar sensitivities.

The similar results for the sensors A1 to A8, except A7, are expected since they are made of the same materials and have bi-material legs of the same dimensions, apart from A5. Sensor A5 has longer bi-material legs, a property which according to Equation (1) should have increased its thermomechanical sensitivity. This result allows us to conclude that the longer bi-material legs, which are top-connected to the absorbing area, do not contribute to the increase in sensitivity as much as was expected. Further studies are required for a better explanation. Sensor A7 exhibits almost no sensitivity, as expected and explained in Section A of this chapter.

Sensor A8 has the same bi-material characteristics; however, it showed lower sensitivity. The most relevant difference that could affect its response is the leg configuration that causes a greater intrinsic bending due to stress. This could be acting in opposition to the thermal deformation. Further studies are required for a better explanation.

Among the sensors of the same configuration, sensor A4 seems to have a slightly higher sensitivity.

3. RESPONSIVITY MEASUREMENTS

Responsivity measurements were performed using the experimental setup, as shown in Figure 10. In this case, the angular displacement of the sensors was measured under 3.8 THz-QCL excitation.

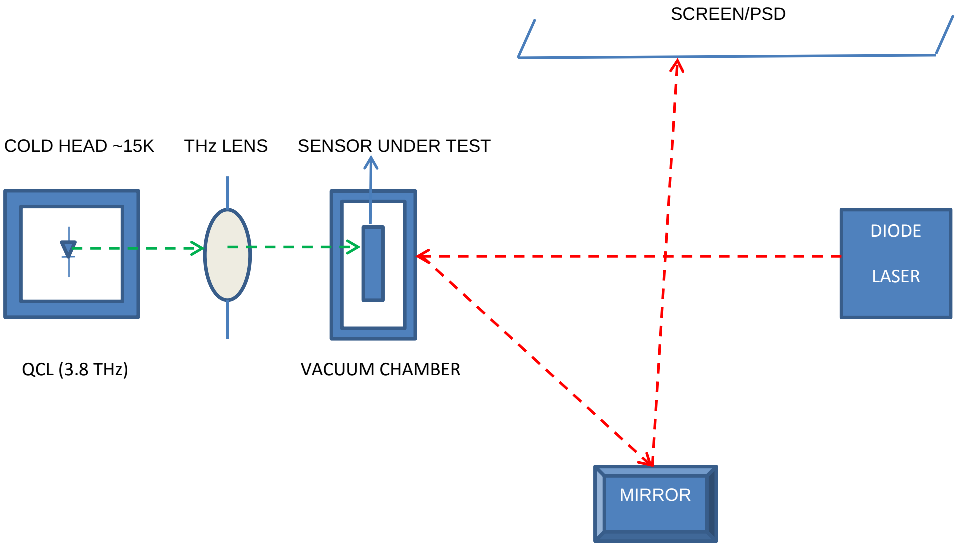

Figure 10. Schematic diagram of the experimental setup used for responsivity measurement. The power of the QCL varied from 0 to approximately 1.5 *μW and in the case of A7 up to 16μW.*

The detector was placed in a vacuum chamber, in which the left window is made of Tsurupica Ⓣ and the right is made of quartz. Heat loss due to convection is dependent on the pressure of the surrounding gas and can be minimized by operating the detector at a relatively low pressure [2]. Hence, the pressure in the vacuum chamber was set approximately to 0.03 *mTorr.* The QCL was placed in the cryostat, which also has a Tsurupica window, and the operating temperatures were between 11 and 20 K. The THz beam passes through a converging 40 mm polyethelene lens (focal length = 100 mm) and hits the THz sensor, placed at the focal point. Both Tsurupica and polyethelene exhibit reasonable transmission (~65%) at 3.8 THz frequency. The mount of the vacuum chamber had three degrees of freedom to allow positioning and fine tuning of the sensors under test.

The same diode laser as that used for the thermal response measurement was used to determine the deflection of the sensor. In this case though, the initial effort was to align the system for each different sensor. This was performed by placing the detector and the intersection point of the two laser beams on the QCL's focal point, to capture most of the QCL power at a single detector. First, the THz laser was turned on, gated at ~200 mHz, and using a CCD camera with coaxial illumination we were able to identify the detector being illuminated by the QCL, inspecting the image and finding the sensors that are excited by the QCL. Then, the diode laser beam was first pointed approximately at the same detector and then fine tuned using the three axis of motion of the mount.

It is important to remark that the vibrations in the chamber, caused by the operation of the vacuum pumps, was significant and the noise in the signal was always present. In many cases, clamps and mounts had to be added in the setup to reduce noise due to the vibrations. In addition, the measurements were repeated several times in order to achieve better accuracy and minimize the error.

The QCL was operated in pulsed mode with frequencies from 1 to 5 kHz while keeping the pulse width at 5 μs. Since the pulse width was kept constant at 5 μs, the average output power is proportional to the pulse frequency.

Since alignment might have been slightly different for different sensors, the absolute power that reaches the sensors (i.e., incident power, P_{in}) is estimated using the responsivity in Equation 6 of Chapter II, along with the calculated thermal conductance using:

$$\theta = \frac{\eta}{G}\frac{d\theta}{dT}P_{in} \tag{9}$$

Responsivity measurements were performed for all the sensors. Figure 11 shows the estimated responsivity for the sensors A1 and A7.

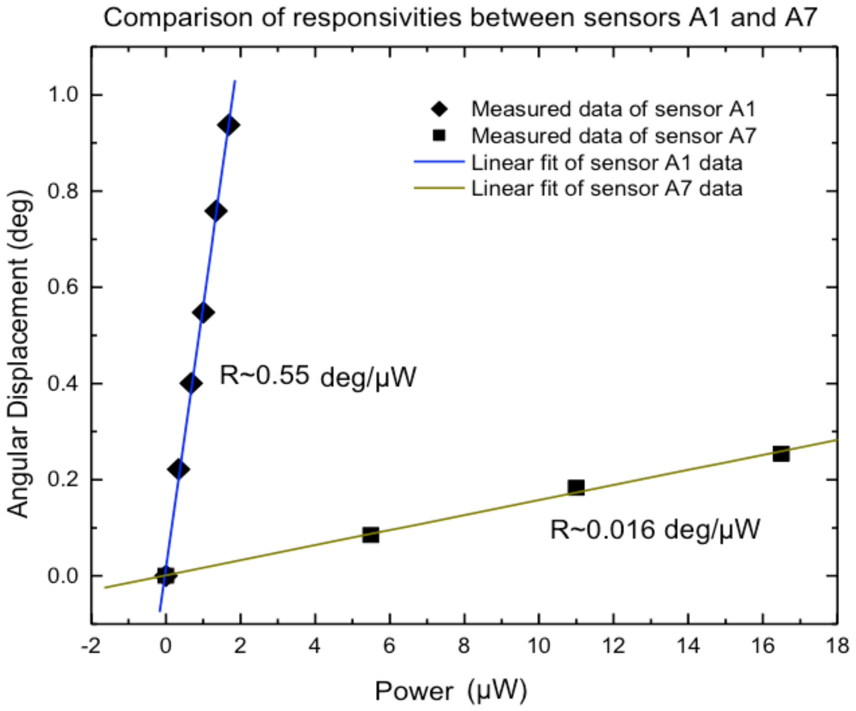

Figure 11. Angular displacement of sensors A1 and A7. Both the sensors have an efficiency coefficient of ~95%. Responsivity of sensor A7, as expected is very small due to the use of two metalized legs on each side.

The solid lines in Figure 11 are linear fits, showing good linearity of the angular displacement for the range of incident power. Note that sensor A7 shows very small response to the incident power. As explained earlier, this is expected since the bi-material legs are compensating the bending of one another. However, the observed responsivity is not zero primarily due to the non-metallic connection between the legs. This causes the temperature on the internal leg (closer to the absorber) to be a little higher than the other's, causing a minute net deflection. This is a good indication that the self-leveling configuration is a sufficient option to reduce the thermal fluctuation noise.

Responsivities of all the sensors are listed in Table 8, along with the theoretical values.

Sensor Property	A1	A2	A3	A4	A5	A6	A7	A8
$d\theta/dP_{meas}$ $\deg/\mu W$	0.55	0.52	0.58	0.53	0.53	0.44	0.016	0.41
$d\theta/dP_{theor}$ $\deg/\mu W$	0.47	0.31	0.47	0.29	0.71	0.37	0	0.43

Table 8. Comparison between theoretical and experimental values of responsivity (*dθ/dP*) of the sensors.

The term $d\theta/dP_{meas}$ represents the experimental value of responsivity and is the slope of the lines in Figures 9 and 11. The term $d\theta/dP_{theor}$ represents the calculated responsivity using Equation (6), with the data from Table 1 for the efficiency η, Table 3 for the thermomechanical sensitivity $d\theta/dT_{theor}$ and Table 4 for the thermal conductance G .

The experimental values of the responsivity for the sensors A1, A3, A6 and A8 are in very good agreement with the theoretical calculations. This is also true for the sensors A2, A4 and A5 but with a little greater divergence. Measured responsivity of the sensor A7 is almost negligible as was expected.

An analysis of the measured results allows the following conclusions:

1. The sensors A1 through A5 have similar thermomechanical sensitivity (same bi-material legs); however, the sensors A2 and A4 have lower efficiency, 64% and 59%, respectively. Therefore, their responsivities are lower than those of sensors A1 and A3, which have 95% efficiency. The fact that the responsivity of A4 is slightly higher than A2's, although it has a lower efficiency, is most likely to be due to limitations of our experimental setup.

   Figure 12 shows the angular deflection of the sensors A2, A3 and A4, highlighting their efficiencies.

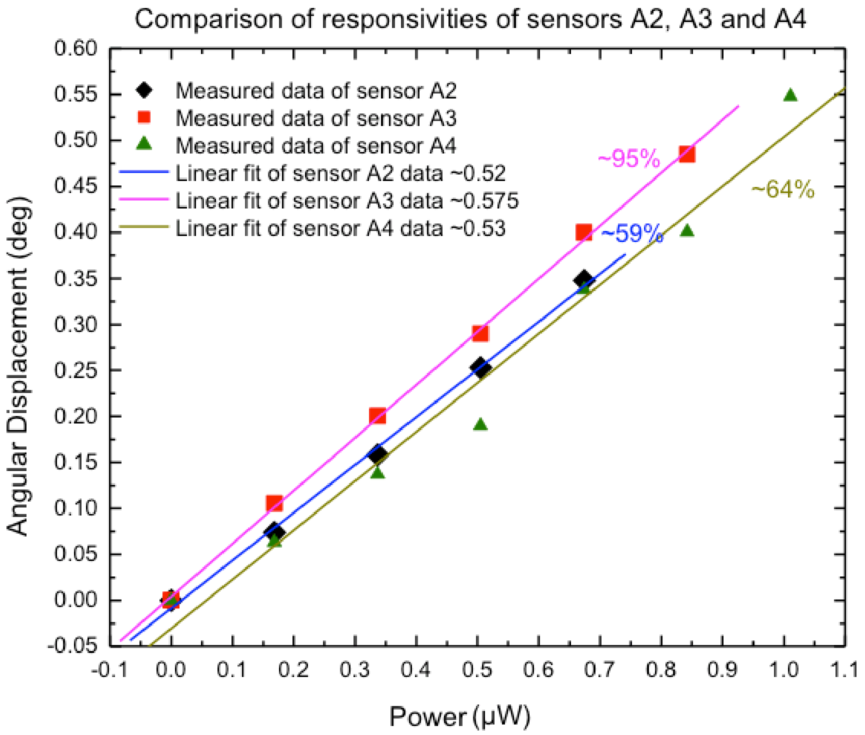

Figure 12. Angular deflections of the sensors A2, A3 and A4. The efficiencies of the sensors are indicated necx to the lines. The slope of each linear fit, which represents the responsivity R, is indicated at the legends.

2. Sensor A5 has a little higher thermomechanical sensitivity than the sensor A1 (longer bi-material legs); however; it has a smaller absorption area, and the overall trade gives a smaller responsivity.

3. Sensor A6 has 95% efficiency; however, since the anchors are smaller than in the other sensors, the thermal conductance G is higher. Therefore, its responsivity is lower than that of A1 and A3, as expected.

4. Sensor A7 has almost no thermomechanical response; therefore, even though its efficiency is 95%, the responsivity is almost negligible, as expected.

5. Sensor A8 should have thermomechanical sensitivity similar to that of sensor A1, which has been confirmed in the previous sets of measurements (see Table 7). The thermal conductivity is shown to be between that of sensors A1 and A6 (see Table 5) due to the anchor configuration. Responsivity measurements show a value lower than that of A1 and A6, which is not expected. However, the measured value has a very small deviation from the theoretical one, which confirms the sufficient measurements of responsivity.

4. SPEED OF OPERATION

For the measurement of speed of operation of the sensors, a position sensing detector (PSD) instead of the screen used earlier was employed to allow measurement of smaller deflections. The PSD is a quadrant photodiode, as shown in Figure 13.

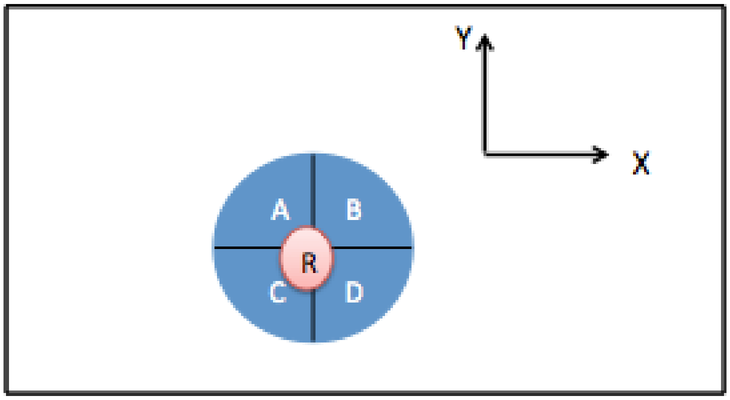

Figure 13. Quadrant photodetector. The A, B, C, and D are the four quadrants and R is the radius of the reflected laser beam from the bi-material sensors. The position of the beam (X,Y) is calculated using the responses of the four detectors using: $X=\frac{(B+D)-(A+C)}{A+B+C+D}$ and $Y=\frac{(A+B)-(C+D)}{A+B+C+D}$, where *A*+*B*+*C*+*D* is the total power of the beam [23] . Initially, the beam is centered by adjusting position of the laser beam.

For optimum performance and resolution, the spot size should be as small as possible, while being bigger than the gap between the photodetectors. When illuminated, the cells generate an output signal proportional to the intensity of the illumination. The output signal is then digitized and processed by a computer. The software performs basic calculations of the position and power of the beam. The output position is displayed as a fractional number or as a percentage, where the percentage represents the fraction of the beam movement relative to the X and Y direction [23]. In our case, the sensor was deflected from the pulsed THz laser beam and returned to its unperturbed position when the excitation was terminated.

The time constant was measured using two different methods:

The first approach was based on the frequency response of the sensor, which was obtained by sweeping the QCL gating frequency from 100 mHz to 30 Hz under the same incident power and recording the output peak to peak signal of the PSD. The normalized frequency response of sensor A1 is plotted in Figure 14. The time constant was obtained from this graph by taking the inverse of the 3 dB frequency (70.7% of the normalized amplitude), as in

$$\tau = 1/2\pi f_{3dB} \tag{12}$$

The second approach used the transient response of the sensor. The time constant in this case was obtained by measuring the time at which the normalized output signal is *1–1/e (63.2%):*

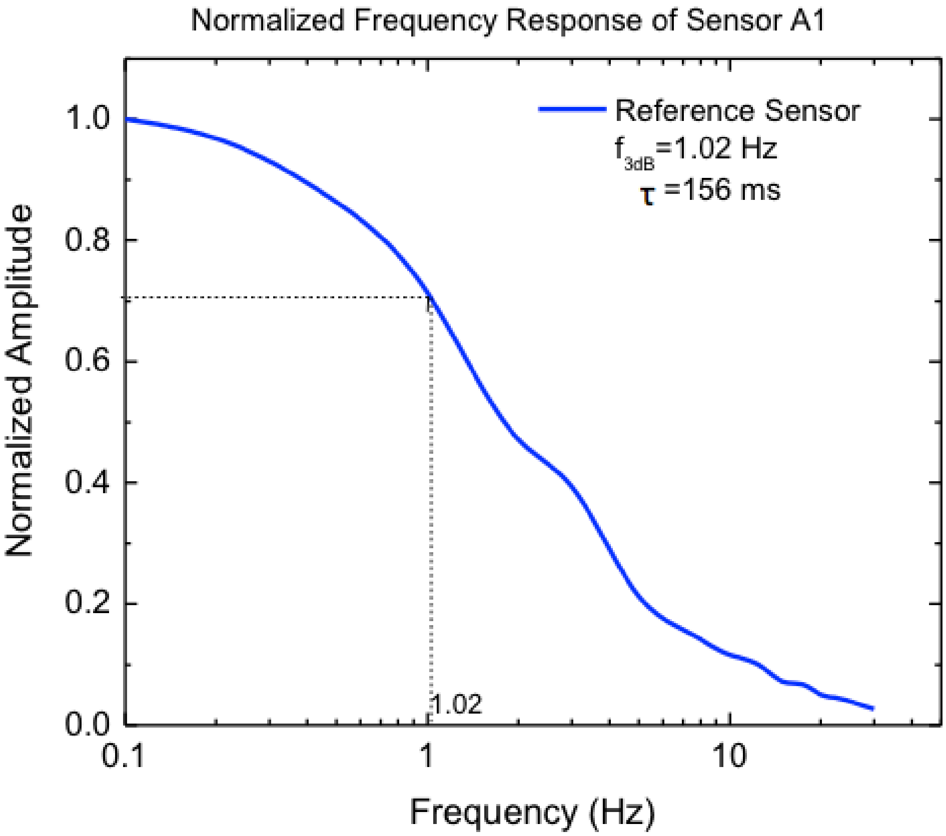

Figure 14. First method to obtain the speed of operation of the sensor A1. The graph is the result of a spline averaging fit of the peak to peak output of the PSD. The 3*dB,* which corresponds to the 70.7 % of the normalized frequency was used to obtain the cut-off frequency, f_{3dB} . Figure 15(a) shows the temporal response of sensor A1, and Figure 15(b) shows one cycle used to extract the time constant.

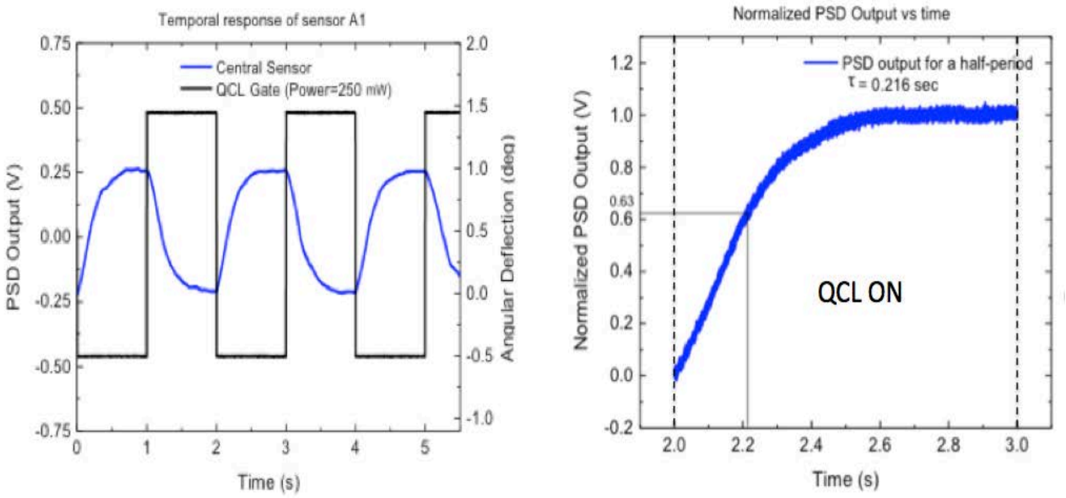

(a) (b)

Figure 15. Temporal response of the sensor A1 by gating the THz-QCL at 0.5 Hz. (a) PSD output signal for several periods. (b) Normalized half-period (1 sec) of the output signal. The time constant was obtained using the time to reach the 63% of the steady state signal.

The same process was repeated for the rest of the sensors. The noise from the mechanical vibrations of the vacuum chamber made the measurements relatively difficult. The experimental values of individual time constants along with the calculated ones are listed in Table 9.

Sensor *Property*	*A1*	*A2*	*A3*	*A4*	*A5*	*A6*	*A7*	*A8*
Frq domain *(ms)* (3*dB*)	0.156	0.165	0.159	0.183	0.121	0.085	--	0.096
Time domain *(ms)* Transient Response	0.216	0.226	0.160	0.181	0.249	0.140	--	0.157
Avg Exp $\tau(ms)$	0.186	0.196	0.160	0.182	0.185	0.113	--	0.127
Theoretical $\tau(ms)$	0.35	0.35	0.35	0.35	0.34	0.24	0.08	0.27

Table 9. Comparison between theoretical and experimental values of time constant of the sensors. The average experimental values are based on the average of the two different methods employed.

The experimental values are generally in agreement with the theoretical values. The divergence between them is almost the same for all the sensors, a fact which allows us to assume that the measurements were correct.

An analysis of the measured results allows the following conclusions:

1. The sensors A1 to A5 have a similar temporal response, which is expected since they have the same anchor configuration and therefore the same thermal conductance G. The size of the square elements for sensors A2 and A4 (19x19 and 17x17 μm^2 respectively) is not affecting the time constant, as was expected. However, sensor A3 was expected to have exactly the same response as A1, which has not been verified. This may be due to limitations in our experimental setup and measurements and should be repeated in a future work.
2. The experimental results using the two methods for sensor A5 have a significant difference between them. We assume that the

transient method is more accurate, because it is closer to the theoretical value. Sensor A5 has longer bi-material legs which is probably the reason for the higher time constant.

3. Sensor A6 has a lower time constant. This is expected due to its smaller total size of the anchor, which increases the thermal conductance and hence reduces the time constant.
4. For sensor A7, it was impossible to obtain results using either of the methods described due to its very low sensitivity.
5. Sensor A8 should have a lower time constant than A1's, which is confirmed by the experimental results. This is due to the smaller absorbing area, which decreases the total thermal capacitance but also due to its smaller anchor area which increases the total thermal conductance of the sensor.

5. NOICE EQUIVALENT POWER (NEP)

The NEP was also determined using the PSD to read the deflection as the THz power is decreased. Figure 16 shows the PSD signal corresponding to minimum detectable THz power, including the readout noise for sensor A1, taken from [2]. The fact that the influence of readout cannot be eliminated from the experimental results makes it difficult to compare the experimental and the theoretical values (estimated to be between 5 to 15 pW [2]).

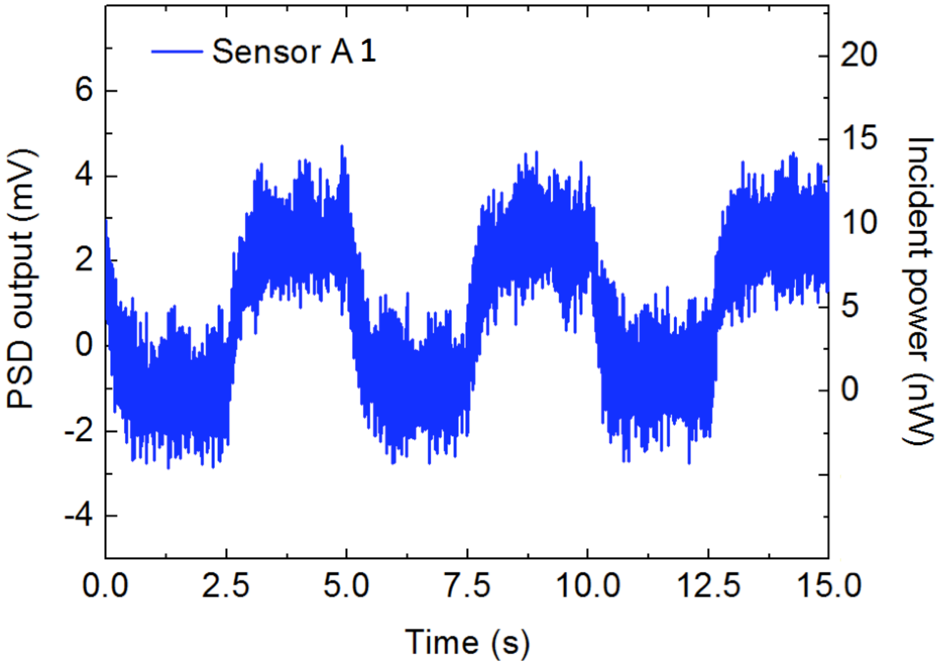

Figure 16. Measured Output voltage of the PSD for the sensor A1 by gating the QCL at 200 mHz. The estimated power incident on the detector is shown on the right vertical axis. From [2].

The measured NEP values for all the sensors are listed in Table 10.

Sensor *Property*	*A1*	*A2*	*A3*	*A4*	*A5*	*A6*	*A7(μW)*	*A8*
$NEP_{meas}(nW)$	10	41	20	122	59	40	4.4	--

Table 10. Experimental values of the minimum detectable incident power.

Since the measured values of minimum detectable incident power is in the order of tenths of nW, which is three orders of magnitude higher than the predicted intrinsic values [2], it is reasonable to assume that most of the noise is originated from the experimental setup. Vacuum chamber vibrations, QCL fluctuations, readout laser fluctuations, PSD noise, oscilloscope limitations, etc., are by far limiting the overall performance. The NEP value for the sensor A4 was measured to be much higher than the rest potentially due to high background vibrations in the laboratory environment.

C. GENERAL DISCUSSION: ANALYSIS AND OPTIMIZATION

According to Table 8, the sensors A1 and A3 show the highest responsivities. Sensors A2 and A4 also have high responsivity, although their absorption efficiency is lower than the A1 and A3, due to the smaller square size. Moreover, Table 8 shows a significant decrease of responsivity for sensor A6, when shifting from the configuration of anchor of A1 to a high thermal conducting configuration. Therefore, it is concluded that the configuration of sensor A1 provides the optimum responsivity for used with 3.8 THz QCL.

The current sensors are too slow for real time imaging; however, it is possible to reduce the pixel size to increase the speed of operation for real time imaging applications.

IV. CONCLUSION

In this thesis a set of bi-material THz sensors with integrated metamaterial absorbers was characterized. The characterization includes both the structural properties as well as figures of merit. The measured figures of merit include thermal time constant, responsivity, speed of operation and minimum detectable THz power.

The measurements showed a responsivity of up to 0.6 *deg/μW* and time constants as low as 113 *ms.* Moreover, the minimum detectable power was measured to be as low as 10 *nW*. It is possible to scale the existing bi-material sensor designs to increase the speed of operation needed for real time THz imaging. For example, decreasing the absorbing area by 10 to 20%, increasing the length of the bi-material legs by 10 to 15% and decreasing of the thermal insulating anchor size by 50 to 60%, is estimated to improve the speed of operation while maintaining the responsivity at the same level. The square size of the element should remain the same, as well as the materials used for matching the 3.8 THz QCL frequency.

In future research it is important to make improvements to the experimental setup, such as the use of a larger vacuum chamber to provide better access to the sensors and reduction of mechanical vibrations generated by the cryostat and vacuum pumps. In addition, the optical readout system needs to be optimized using a stable light source and low noise electronics. These enhancements will allow the determination of intrinsic noise of detectors and high sensitive imaging.

THIS PAGE INTENTIONALLY LEFT BLANK

REFERENCE LIST

[1] C. Bolakis, “High terahertz absorbing nanoscale metal films for fabrication of micromechanical bi-material THz sensors,” M.S. Thesis, Physics Dept., NPS, Monterey, CA, 2010.

[2] F. Alves, D. Grbovic, B. Kearny, N. V. Lavrik, G. Karunasiri, “Bi-material terahertz sensors using metamaterial structures,” *Optics Express*, vol. 21, pp. 1–16, Feb. 2013.

[3] D. Grbovic, F. Alves, B. Kearney, K. Apostolos, G. Karunasiri, “Optimization of THz absorption in thin films,” *Sensors, 2011 IEEE*, pp.172,175, 28–31, Oct. 2011.

[4] R. M. Langdon, V. Handerek, P. Harrison, H. Eisele, M. Stringer, C. F. Rae, M. H. Dunn, “Military Applications of Terahertz Imaging,” presented at 1st EMRS DTC Technical Conference, Edinburgh, 2004.

[5] J. F. Federici, B. Schulkin, F. Huang, D. Gary, R. Barat, F. Oliveira, and D. Zimdars, “THz imaging and sensing for security applications–explosives, weapons, and drugs,” *Semicond. Sci. Technol.* 20(7), S266–S280 (2005).

[6] S. M. Kim, F. Hatami, J. S. Harris, A. W. Kurian, J. Ford, D. King, G. Scalari, M. Giovannini, N. Hoyler, J. Faist, and G. Harris, “Biomedical terahertz imaging with a quantum cascade laser,” *Appl. Phys. Lett*. 88(15), 153903 (2006).

[7] P. F. Taday, I. V. Bradley, D. D. Arnone, M. Pepper, “Using Terahertz Pulse Spectroscopy to study the crystalline structure of a drug: A case study of the polymorphs of ranitidine hydrochloride,” *J. Pharmaceutical Sciences* 92(4), pp. 831–838, 2003.

[8] M. C. Kemp, P. F. Taday, B. E. Cole, J. A. Cluff, A. J. Fitzgerald, W. R. Tribe, “Security applications of terahertz technology,” *Proc. of SPIE* Vol. 5354, pp. 1–9.

[9] F. Alves, D. Grbovic, B. Kearney, and G. Karunasiri, “Microelectromechanical systems bi-material Terahertz Sensor with Integrated Metamaterial Absorber,” *Opt. Lett.* 37(11), 1886–1888 (2012).

[10] R. H. Clothier and N. Bourne, “Effects of THz exposure on human primary keratinocyte differentiation and viability,” *J. Biol. Phys.* 29(2/3), 179–185 (2003).

[11] E. Montagner, “Optical Readout System for Bi-Material Terahertz Sensors” M.S. Thesis, I.S. Dept., NPS, Monterey, California, 2011

[12] A. W. M. Lee, B. S. Wil, S. Kumar, Qing Hu, and J. L. Reno, “Real-time imaging using a 4.3-THz quantum cascade laser and a 320x240 microbolometer focal-plane array,” *IEEE Photon. Technol. Lett.* 18(13), 1415–1417 (2006).

[13] B. N. Behnken, G. Karunasiri, D. R. Chamberlin, P. R. Robrish, and J. Faist, “Real-time imaging using a 2.8 THz quantum cascade laser and uncooled infrared microbolometer camera,” *Opt. Lett*. 33(5), 440–442 (2008).

[14] Q. Zhang, Z. Miao, Z. Guo, F. Dong, Z. Xiong, X. Wu, D. Chen, C. Li, and B. Jiao, *Optoelectron. Lett.* 3, pp. 119 (2007).

[15] H. Tao, N. I. Landy, C. M. Bingham, X. Zhang, R. D. Averitt, and W. J. Padilla, *Opt. Express* 16, pp. 7181 (2008).

[16] F. Alves, B. Kearney, D. Grbovic, N. V. Lavrik, and G. Karunasiri, “Strong terahertz absorption using SiO2/Al based metamaterial structures,” *Appl. Phys. Lett.* 100(11), 111104 (2012).

[17] B. Kearney, F. Alves, D. Grbovic, and G. Karunasiri, “Al/SiOx/Al single and multiband metamaterial absorbers for terahertz sensor applications,” *Opt. Eng.* 52(1), 013801 (2013).

[18] S. Timoshenko, “Analysis of bi-metal thermostat,” *J. Opt. Soc. Am.* 11(3), 233–255 (1925).

[19] H. Budzier, G. Gerlach, *Thermal Infrared Sensors, Theory, Optimization and Practice*, New Jersey: Wiley, 2011, pp 154–165.

[20] D. Grbovic, N. V. Lavrik, S. Rajic, and P. G. Datskos, “Arrays of SiO2 substrate-free micromechanical uncooled infrared and terahertz detectors,” *J. Appl. Phys.* 104(5), 054508 (2008).

[21] E. L. Dereniak, G. D. Boreman, *Infrared Detectors and Systems,* New Jersey: Wiley, 1996.

[22] P. W. Kruse, *Uncooled Thermal Imaging, Arrays Systems and Applications*. Bellingham, WA: SPIE Press, 2002.

[23] *Position Sensing and Alignment Engineering Guide*, Duma Optronics, Ltd., Nesher, Israel, 2011, pp. 1–2, 8–9.

INITIAL DISTRIBUTION LIST

1. Defense Technical Information Center
   Ft. Belvoir, Virginia

2. Dudley Knox Library
   Naval Postgraduate School
   Monterey, California